Detection of Martian dust clouds by SPICAM UV nadir measurements during the October 2005 regional dust storm

N. Mateshvili [a],*, D. Fussen [a], F. Vanhellemont [a], C. Bingen [a], J. Dodion [a], F. Montmessin [b], S. Perrier [b], J.L. Bertaux [b]

[a] *Belgian Institute for Space Aeronomy, Avenue Circulaire-3, B-1180 Brussels, Belgium*
[b] *Service d'Aeronomie (CNRS), Riduit de Verrieres – BP 3, Route des Gatines, 91371 Verrieres le Buisson Cedex, France*

Abstract

The SPICAM UV spectrometer onboard Mars Express observed two regional dust storms: on October 24, 2005, near Argyre Planitia and on July 9, 2005, in Hellas Planitia. The measurements were performed in nadir mode. The spectral domain 210–310 nm is considered. A comparison with a prior orbit which passed above almost the same path 6 days before the storm near Argyre Planitia has shown a significant decrease of the radiance factor. The difference grows at shorter wavelengths and shows significant dust absorption in the UV. The data have been used to retrieve the dust optical thickness τ, single scattering albedo w and asymmetry factor g. The fitting of the spectra by a radiative transfer code has revealed a set of solutions which could be constrained by Mie modeling of the parameters τ, w, and g for a gamma particle size distribution. The following estimates of the dust optical parameters are obtained: $w = 0.64 \pm 0.04$ at $\lambda = 300$ nm and decreases to 0.6 ± 0.045 at 213 nm, $g = 0.86 \pm 0.03$ at 300 nm and slightly grows to 0.88 ± 0.04 at 213 nm, $\tau = 2.5 \pm 0.5$ for the first dust event and $\tau = 2.0 \pm 0.5$ for the second one. The obtained values of single scattering albedo are consistent with the Hubble Space Telescope and Mariner 9 results.
© 2007 COSPAR. Published by Elsevier Ltd. All rights reserved.

Keywords: Martian atmosphere; Optical properties; Dust; Aerosols

1. Introduction

Mineral dust is an important component of the Martian atmosphere. The optically thin atmosphere is abundant of dust which serves as condensation nuclei in the process of formation of Martian ice clouds. It is also a significant source of diabatic heating by absorbing visible and ultraviolet radiation and emitting in the infrared. The dust affects vertical temperature profiles and causes local temperature gradients. Surface winds induced by the temperature gradients lift more dust into the atmosphere leading to formation of regional and sometimes global dust storms which can have a significant effect on general circulation patterns (Cantor et al., 2001).

Dust optical properties in the UV are not well known although this wavelength domain is important for correct climate modeling as well as for correct estimates of the amount of the UV radiation reaching Martian surface. In the conditions of a thin and variable Martian ozone layer, dust may play a significant role as a UV absorber and it should be taken into account in estimations of the Martian surface habitability. The correct knowledge of the dust optical properties in the UV is also important for the retrieval of any other species such as ozone or cloud optical thicknesses and for correct estimates of the Martian surface albedo.

The key parameters that determine the dust optical properties are dust single scattering albedo and asymmetry factor. These parameters are closely connected to the dust particle size distribution and the wavelength dependent complex refractive index. The knowledge of the dust

---

* Corresponding author.
  E-mail address: ninam@aeronomie.be (N. Mateshvili).

refractive index allows to draw some conclusions about the nature of the dust material.

The main information about Martian dust UV optical properties comes from Mariner 9 UV measurements and Hubble Space Telescope (HST) observations. Pang et al. (1976) and Pang and Ajello (1977) analyzed spot pointing measurements performed by Mariner 9 during the 1971 dust storm in the wavelength domain 210–350 nm. They concluded that the Martian dust has a high refractive index and is strongly absorptive in the UV. Wolff et al. (1999) analyzed HST observations of a regional dust storm in Valles Marineris. The results were further discussed in Clancy et al. (1999).

The SPICAM instrument onboard Mars Express performed numerous nadir measurements in the UV during the period from January 2004 to July 2006 corresponding to the Martian year (MY) 27 and the beginning of the MY28 (Clancy et al., 2000). In this work, we consider two SPICAM orbits. They were acquired on October 2005, when the regional dust storm was observed by HST and ground-based telescopes and on July 9, 2005, when the storm in Hellas Planitia was registered by MOC (Mars Orbiter Camera). We discuss some dust optical properties which can be derived from the analysis of these two dust storms observed by SPICAM.

2. The SPICAM instrument

SPICAM is a spectrometer onboard Mars Express. It has two channels tuned to spectral ranges in the UV and in the IR. The UV channel covers the domain of wavelengths 118–320 nm with an average resolution of 0.5 nm. The light is collected via a slit and registered by the CCD array with spectral scanning along one dimension and spatial scanning along the other. The data are binned by four pixels due to telemetry constraints that reduced the spatial resolution. Finally, five spectra are transmitted every second, covering slightly different areas. The spectra have average resolution of 1.2 km across the track and 2.4 km along the track in nadir mode (Perrier et al., 2006). A detailed description of the instrument can be found in Bertaux et al. (2006).

3. Measurements

The SPICAM UV channel spectral range contains a strong absorption band of CO_2 within 118–200 nm, and the ozone Hartley band within the range 220–280 nm. In nadir mode, besides of these two main absorbers, many surface features manifest themselves as variations of the UV albedo. Martian soil contains minerals with high abundance of iron oxides and therefore the surface has low UV albedo (Bell, 1996). Water ice clouds are bright in UV and are well contrasted against this dark background (e.g. Wolff et al., 1999). The way how dust clouds should manifest themselves in UV strongly depends on magnitude and

wavelength dependence of their optical parameters such as the single scattering albedo and the asymmetry factor.

Here, we have chosen two prominent dust storms, the existence of which is confirmed independently, to investigate the optical properties of these dust clouds.

According to the HST observations (http://hubblesite.org/newscenter/archive/releases/2005/34/image/b) and the ground-based telescopic observations of British Astronomical Association (McKim, 2006), a regional dust storm started in October 2005 over Chryse Planitia and then extended southward. This dust storm was briefly considered in Mateshvili et al. (2007) (hereafter Paper I) and here we analyze it in detail. On October 24 SPICAM crossed the storm at the east of Argyre Planitia (orbit 2284, Fig. 1). This episode of the dust storm was also registered by ground-based telescopic observations (inset in Fig. 1, J. Warren, http://marswatch.amaonline.com/mars_images_2003a.htm).

The second dust storm was registered by Mars Orbiter Camera (Malin et al., 2006) in Hellas basin at $L_s = 245°$ (July 9, 2005, orbit 1902). The MOC images were obtained in two spectral channels – blue (400–450 nm) and red (575–625 nm). Comparing red and blue MOC images, Cantor et al. (2001) were able to detect numerous dust storms. The storms manifested themselves as prominent enhancement of the registered brightness in red images and less prominent in blue ones. Fig. 2 presents MOC wide-angle red image acquired at $L_s = 245°$. The dust storm in Hellas is clearly visible.
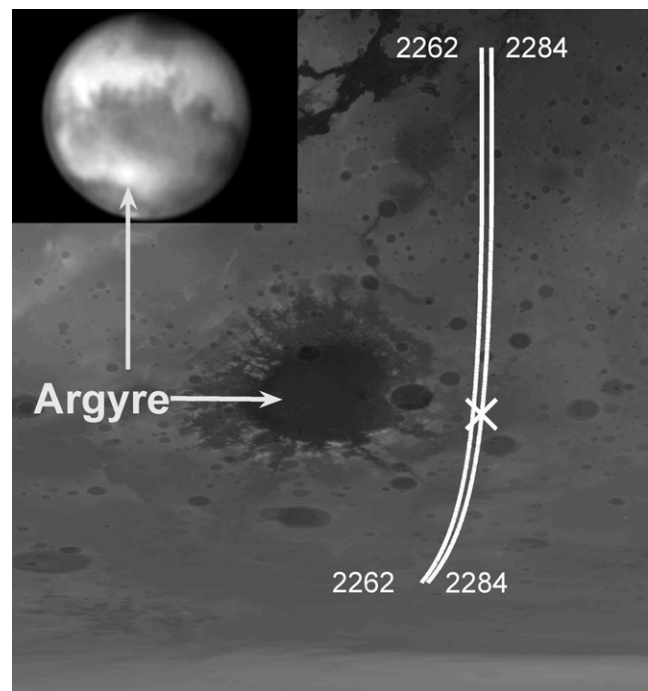

Fig. 1. Tracks of orbits 2262 and 2284 superimposed on Mars Laser Altimeter map. The position of the October 24, 2005, dust storm maximum is marked with a cross (see Fig. 3). The inset presents a telescope image of Mars (red filter) obtained on October 24, 2005, by Joel Warren, Amarillo, TX; the dust storm is clearly visible as a white strip in the southern hemisphere (the South pole is in the bottom of the image).
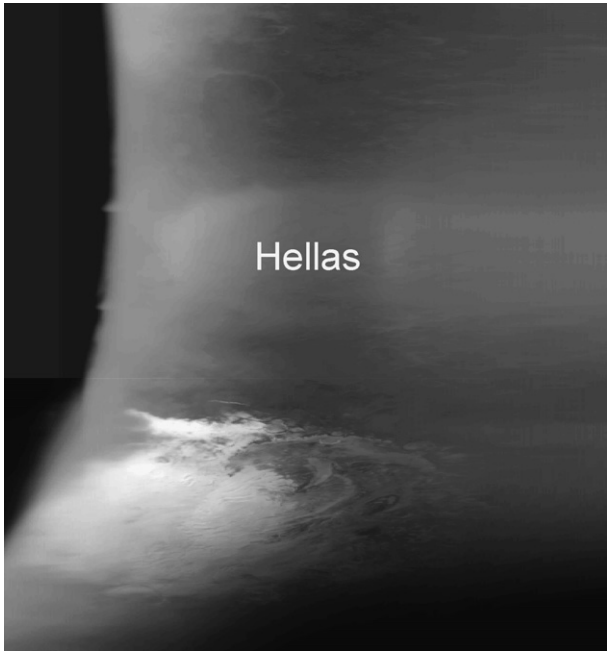
Fig. 2. MOC red image (S0800921) which was acquired in the same day as the orbit 1902 (July 9, 2005). The dust storm in Hellas is clearly visible.

We start our analysis by consideration how dust should manifest itself in the UV: whether should it increase or decrease the radiance factor (see Section 4 for the definition of the radiance factor). According to the MOC results, a presence of dust causes an increase of observed brightness in visual diapason but it is not obvious how dust should manifest itself in the UV. We consider the October 24 storm at the east of Argyre Planitia (orbit 2284) to clarify it. A comparison with a prior orbit above almost the same path 6 days before (Fig. 1, orbit 2262) has shown a significant difference in radiance factor before and during the storm. Fig. 3 shows two spectra taken almost above the same area (cross in Fig. 1), one in the presence of the dust
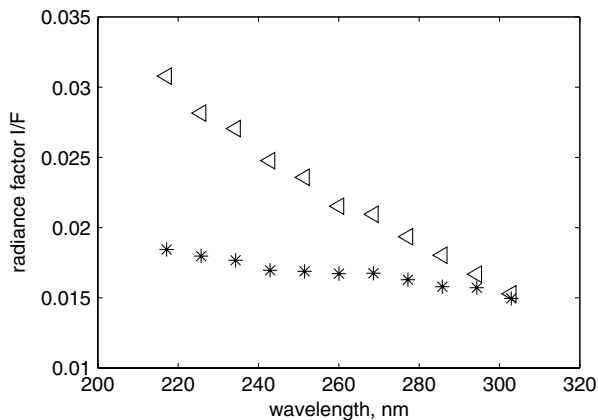

Fig. 3. SPICAM spectra acquired above one and the same area (marked with a cross at Figs. 1 and 3) from orbit 2262 (triangles) and orbit 2284 (asterisks). The data are spectrally averaged over 10 nm. The corresponding observational geometry for the orbit 2284 is: SZA = 37.9°, emission angle 0.07°, and phase angle 38.15°.
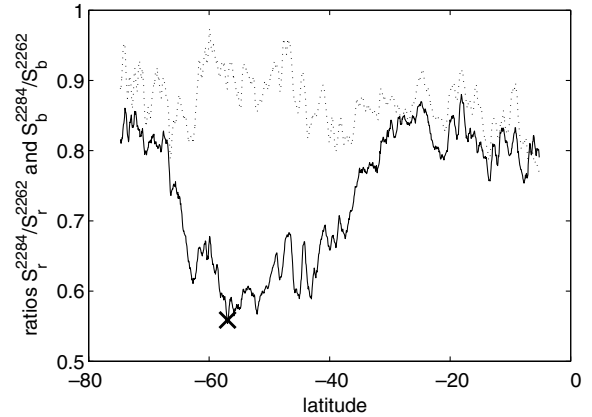

Fig. 4. Ratios between the 'red' sub-domains S_r for orbits 2284 and 2262 (dotted line) plotted in Fig. 1, and the 'blue' sub-domains S_b for the same orbits (solid line). The maximal dust loading point is marked with a cross.

cloud (asterisks, orbit 2284) and the other attributed to the reference orbit 2262 (triangles). The observational geometry, i.e. solar zenith angle (SZA), emission angle η and relative azimuth of scattering ψ are very similar for both the spectra. The presence of dust caused a clear decrease of the radiance factor. The difference between the two spectra is very small at 300 nm and grows at shorter wavelengths showing significant absorption in the UV. Both the data sets were acquired during the southern summer (solar longitude $L_s = 308$ for orbit 2262 and $L_s = 312$ for orbit 2284). By this time the Martian ozone layer disappears in the southern hemisphere (e.g. Perrier et al., 2006 and references therein) and dust is the only possible absorber in the considered UV range.

To locate the dust storm, the following comparison between orbits 2284 and 2262 was made. The measured spectra were averaged within two 10 nm sub-domains: 'red' (S_r), centered at 300 nm and 'blue' (S_b), centered at 213 nm. S_r and S_b were considered as functions of latitude ϕ. To reduce the measurement noise, $S_r(\phi)$ and $S_b(\phi)$ were smoothed using local polynomial approximation. Fig. 4 shows the ratios $R_r = S_r^{2284}/S_r^{2262}$ (dashed line) and $R_b = S_b^{2284}/S_b^{2262}$ (solid line) as a function of latitude. We can see that the dust storm manifests itself as a deep minimum on the $R_b(\phi)$.

Below we try to fit the S_r and S_b values by a radiative transfer code to obtain some estimates of the dust optical parameters.

4. The retrieval procedure

The model of the Martian atmosphere used in this paper is described in Perrier et al. (2006). Some peculiarities and principles of ice and dust cloud detection are presented in Paper I. Here, we will mention only some important details. The spectrometer was calibrated by using SPICAM UV measurements of bright stars out of the atmosphere. The raw data were converted to the radiance factor I/F. πF is the solar flux at the top of the atmosphere at the

particular wavelength and I is light intensity scattered in the direction of observation. After the calibration the data are expressed in radiance factor I/F. The plain-parallel multiscattering radiative transfer code SHDOM (Evans, 1998) was used for the modeling.

We use the 300 nm Martian albedo map from Paper I which has been obtained as a result of statistical processing, after excluding the parts of orbits contaminated by ice clouds. In Paper I, we came to the conclusion that the Martian surface albedo can be considered as lambertian only with some restrictions. For phase angles (angles between the incident and scattered beams) less than 25° albedo essentially increases due to the opposition effect (Hapke, 1986). The procedure of the surface albedo correction for the opposition effect is described in Paper I.

The surface pressure, the surface temperature, and the temperature profiles were taken from the GCM calculations (Forget et al., 1999), and the pressure profiles were calculated using the hydrostatic equation.

The dust extinction vertical profile becomes an important issue in case of high values of the optical thicknesses that are expected in the dust storm conditions. Here, we use the profile proposed by Conrath (1975):

$$\beta(h) = \beta_0 \exp(\gamma(1 - p_0/p(h))) \qquad (1)$$

where h is the altitude above the surface, β is the dust extinction coefficient, p is the pressure, γ is a parameter. The index 0 corresponds to the values of these quantities on the surface level. Fig. 5 shows dust extinction profiles with different γ. For the future analysis we use $\gamma = 0.04$, a reasonable value for average Martian dust extinction profile as shown by Montmessin et al. (2006), although we should keep in mind that in conditions of a dust storm this parameter may change.

In the next section, we compare the retrieved dust optical parameters with the modeled ones. For the dust optical parameter modeling the gamma dust particle size distribution was used:

$$n(r) = c r^{(1-3v_{eff})/v_{eff}} \exp[-r/(r_{eff} v_{eff})]$$

where r_{eff} is the mean cross-section-weighted radius, v_{eff} is the mean cross-section-weighted variance divided by r_{eff}^2 and c is proportional to the particle concentration. Tomasko et al. (1999) derived the parameters $r_{eff} = 1.6$ μm and $v_{eff} = 0.2$ from Pathfinder images of the Martian sky. Lemmon et al. (2004) derived the value $r_{eff} = 1.5 \pm 0.2$ μm using measurements of Pancam, a high-resolution stereo camera based on the Mars exploration rovers. They used the value $v_{eff} = 0.2$ adopted from Tomasko et al. (1999). Wolff et al. (2006) derived some constrains on dust aerosol by analyzing Mini-TES instrument measurements from the Mars exploration rovers and Mars Global Surveyor TES (Thermal Emission Spectrometer) measurements. They estimated $r_{eff} = 1.2$–1.6 μm for Spirit observational place and 1.4–1.8 μm for Opportunity's one. The value of r_{eff} correlated with the derived optical thickness values. The estimate for v_{eff} was 0.25–0.3.

Fig. 6 presents two gamma distributions with parameters $r_{eff} = 1.6$ μm, $v_{eff} = 0.2$ (solid line), and $v_{eff} = 0.5$ (dotted line). The second one supposes the abundance of small dust particles.

In the dust optical parameters retrieval, the restricted range of considered scattering angles did not allow us to retrieve the real phase function from the measurements. The dust scattering properties were described by the Henyey–Greenstein phase function:

$$P(\cos \theta) = w(1 - g^2)/(1 + g^2 - 2g \cos \theta)^{3/2} \qquad (2)$$

where g is the dust asymmetry factor, w is the dust single scattering albedo and θ the light scattering angle. In this paper, we use the phase angle $\alpha = 180° - \theta$ instead of the scattering angle.

It is not clear that, in our case, the Henyey–Greenstein phase function is a good approximation of the real phase function considering the UV diapason of measurements and the particle sizes cited above. The effective size parameter is

$$x_{eff} = 2\pi r_{eff}/\lambda$$
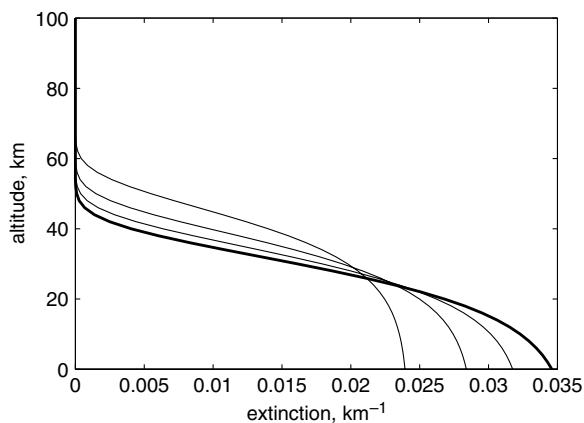

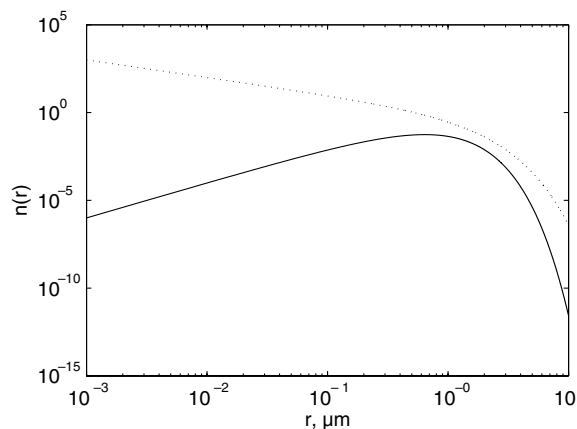Fig. 5. Dust extinction profiles calculated using Eq. (1) for different values of the parameter $\gamma = 0.01$–0.04. The bold line represents the case $\gamma = 0.04$.

Fig. 6. Gamma particle size distribution with parameters $r_{eff} = 1.6$ μm, $v_{eff} = 0.2$ (solid line), and $v_{eff} = 0.5$ (dotted line).

where λ is a wavelength of measurements. The parameter x_{eff} reaches values of 30–40 for the considered range of the r_{eff} values. The Henyey–Greenstein phase function is plausible for much smaller values of x_{eff}.

The other important factor which influences on the shape of the phase function is the particle nonsphericity. Mishchenko et al. (1997) modeled phase functions for both the polydisperse equiprobable shape mixture of prolate and oblate spheroids with x_{eff} varying in the range 2–24 and for spheres, surface-equivalent to them. The important features by which the modeled phase functions for spherical particles differ from the Henyey–Greenstein ones are significant backscatter peaks and much more prominent forward peaks. In case of nonspherical particle shape the phase functions still resemble the Henyey–Greenstein phase function and show only a shallow minimum at right angles although the difference in the forward peak magnitude is rather significant.

For the Martian dust, we should rather suppose nonspherical particle shape. Here, we consider mostly side scattering and the Henyey–Greenstein phase function seems to be an acceptable approximation. The difference in the forward peak between the Henyey–Greenstein phase function and the more realistic one for nonspherical particles should cause some small scaling effect on all optical parameters as it follows from similarity principle (Liou, 2002, Chapter 6.5.3).

5. Dust optical parameters

The main difficulty at the retrieval of the dust optical thickness (τ) from the radiance factor I/F is due to unknown dust optical parameters w and g. If we try to retrieve the three parameters simultaneously, we immediately face the problem that the solution is not unique. The situation is complicated by the presence of uncertainties in the surface albedo and in the dust extinction vertical profile. It should be also mentioned that the surface albedo at the short-wavelength (200 nm) is not well known.

In this section, we try to extract some information about the dust optical properties. The parameters w and g are derived by fitting the measurements with a radiative transfer model and assuming a Henyey–Greenstein phase function. They are compared with the results of the Mie modeling of w and g which was performed for a wide range of complex refractive index using a gamma particle size distribution. The scheme of the analysis is presented in Fig. 7.

The proposed approach is reasonable in conditions of a dust storm when the value of the dust optical thickness is large.

Hereafter, we consider both the dust storm events near Argyre basin (Fig. 1) and in Hellas (Fig. 2) in parallel. From the first one, the measurement M (orbit 2284), marked by cross in Figs. 1 and 4 with the maximal dust loading is chosen for further analysis. The maximal dust loading corresponds to a minimum on the $R_b(\phi)$ dependence (see Fig. 4). From the second dust event (orbit
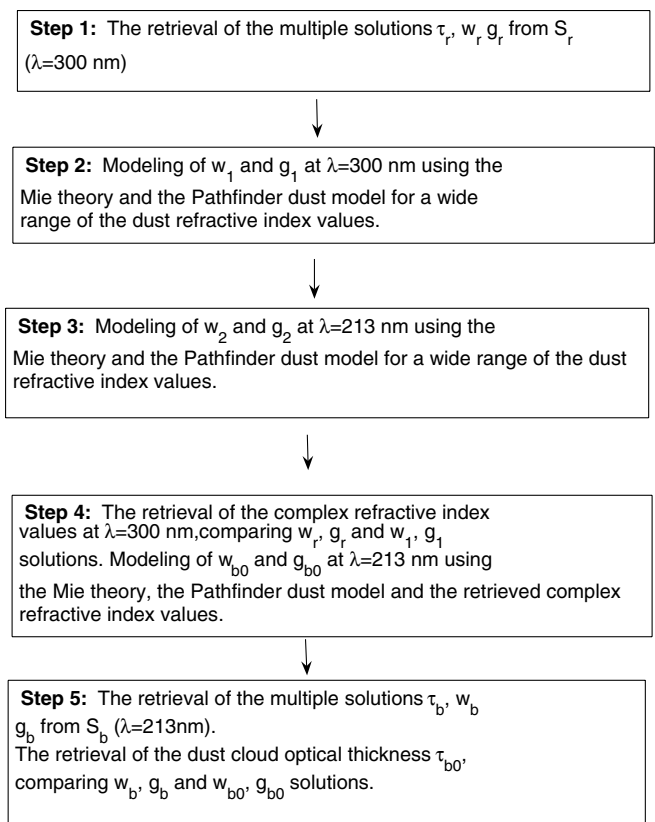
Step 1: The retrieval of the multiple solutions τ_r, w_r g_r from S_r (λ=300 nm)

Step 2: Modeling of w_1 and g_1 at λ=300 nm using the Mie theory and the Pathfinder dust model for a wide range of the dust refractive index values.

Step 3: Modeling of w_2 and g_2 at λ=213 nm using the Mie theory and the Pathfinder dust model for a wide range of the dust refractive index values.

Step 4: The retrieval of the complex refractive index values at λ=300 nm, comparing w_r, g_r and w_1, g_1 solutions. Modeling of w_{b0} and g_{b0} at λ=213 nm using the Mie theory, the Pathfinder dust model and the retrieved complex refractive index values.

Step 5: The retrieval of the multiple solutions τ_b, w_b g_b from S_b (λ=213nm). The retrieval of the dust cloud optical thickness τ_{b0}, comparing w_b, g_b and w_{b0}, g_{b0} solutions.

Fig. 7. A scheme of the analysis performed in this paper. τ, w, and g are dust optical thickness, single scattering albedo and asymmetry factor respectively. S_r and S_b are radiance factors, averaged over 10 nm at wavelengths $\lambda = 300$ nm and $\lambda = 213$ nm.

1902), one of the measurements inside Hellas basin where a high dust loading is expected, was chosen.

First, the value of the radiance factor at 300 nm (S_r) was fitted by the radiative transfer model. The look-up tables of radiance factor I/F were built using a wide range of dust optical parameters τ, w and g (Table 1). The Henyey–Greenstein phase function was used. The 300 nm surface albedo map (Paper I) was used to derive the value of the surface albedo A_r. The observational geometries (values of SZA, η, ψ) and the surface pressure which corresponded to the considered measurements were used.

The look-up tables were examined for the values of I/F which deviated by no more than 5% from the value of S_r for the chosen measurements. The 5% uncertainty corresponds to the random noise error of measurements (Paper I). The corresponding values of the optical thickness τ_r, single scattering albedo w_r and asymmetry factor g_r were considered as the solutions. All solutions with $\tau_r < 1$ were excluded by supposing that in the conditions of a dust storm τ_r must exceed this figure. The results are presented by circles in Fig. 8 (orbit 2286) and Fig. 9 (orbit 1902). The values of τ_r are represented by different intensity of grey color. There are remarkable features: first, g_r increases with w_r and secondly, for a given value of w_r the value of g_r varies with τ_r in a narrow range, i.e. the radiance factor does not change with τ_r significantly. The first feature arises

Table 1
Ranges of the dust optical parameters used for the modeling

	Minimum	Step	Maximum
Dust optical thickness	0.1	0.1	4
Dust single scattering albedo	0.4	0.01	0.7
Dust asymmetry factor	0.6	0.01	0.9
Real part of the refractive index	1.4	0.01	2.2
Imaginary part of the refractive index	0.001, 0.1	0.001, 0.01	0.1, 1

from the fact that g_r and w_r have an opposite influence on I/F. The rise of w_r (i.e. the decrease of absorption) causes the increase of the radiance factor, whereas the strong forward scattering produces a drop of I/F. The second feature, the weak dependence on τ_r, arises from the fact that the way how the Martian dust manifests itself changes with wavelength, going from an increase of brightness in visible spectral range (e.g. Mars Orbital Camera (MOC) measurements, Cantor et al., 2001) to a decrease of brightness in
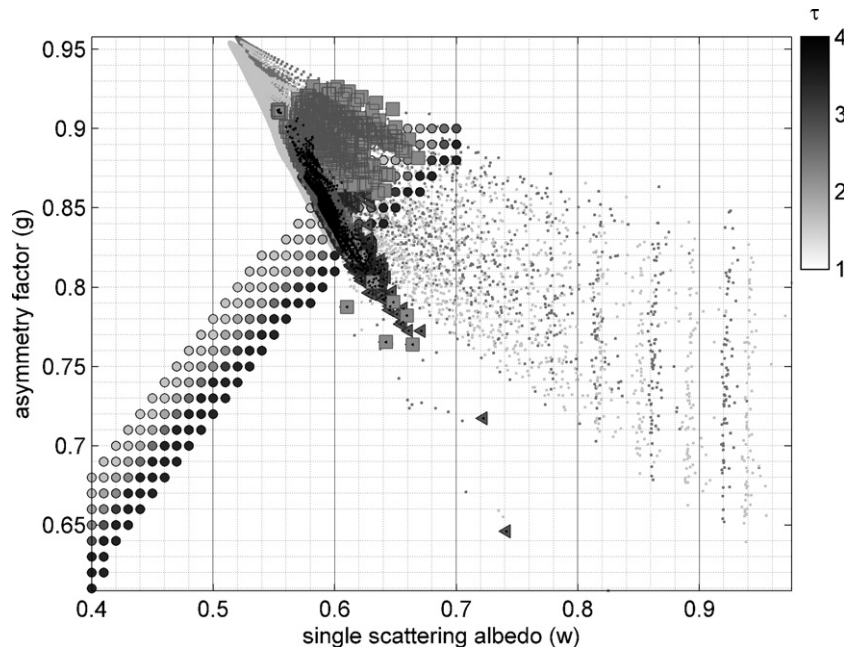

Fig. 8. Orbit 2284: a comparison of the solutions τ_r, w_r, g_r (circles, τ_r increases with the grey color intensity) retrieved from S_r (see Fig. 7, step 1) with results of the Mie modeling w_1 and g_1 (Fig. 7, step 2) at $\lambda = 300$ nm (dark grey dots). The results of the Mie modeling w_2 and g_2 at $\lambda = 213$ nm are presented by light grey dots (Fig. 7, step 3). The dust parameters w_{b0} and g_{b0} at $\lambda = 213$ (Fig. 7, step 4) are presented by squares and triangles. Light grey squares present values of w_{b0} and g_{b0} which correspond to the refractive index with real part $n < 1.8$, dark grey triangles – with $n > 1.8$, black points inside squares and triangle – with imaginary part $k > 0.02$.
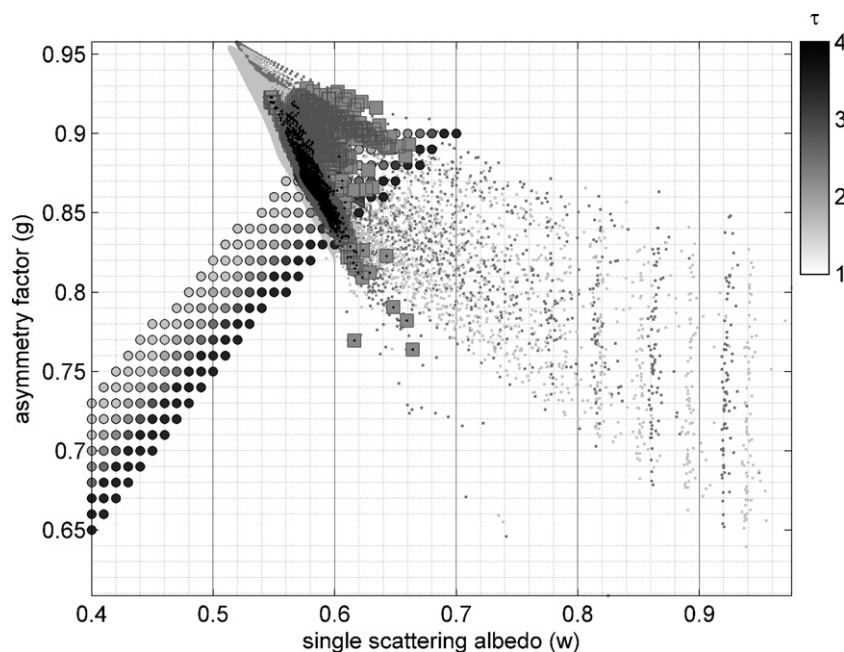

Fig. 9. The same as Fig. 8, for orbit 1902.

the UV (Figs. 3 and 4). At some particular wavelength between these two limits the effect of dust should be minimal. Modeling shows that the wavelength at which these particular conditions will occur depends not only on dust optical properties but also on the surface albedo. Some examples of such influence show MOC images of dust storms above the polar ices, where dust causes a decrease of brightness even in visible diapason (e.g. MOC, image S0800922, Malin et al., 2006).

When comparing the results obtained for orbits 2284 and 1902 (Figs. 8 and 9 correspondingly) the latter exhibits a slight shift towards the larger values of g_r. This shift might appear due to a larger particle size in the deep Hellas basin. The other explanation is that the shift appears due to difference between the real phase function and the adopted Henyey–Greenstein one. This idea is supported by the fact that the phase angles for measurements considered in Figs. 8 and 9 differ significantly (38° and 70°, respectively).

In the second step, the Mie theory was used to model values of single scattering albedo w_1 and asymmetry factor g_1. The purpose of this modeling is to constrain the solutions obtained at the first step of our analysis. The modeling was performed at the wavelength $\lambda = 300$ nm for a wide range of the dust complex refractive index values (Table 1). The dust particle size distribution with parameters $r_{eff} = 1.6$ μm and $v_{eff} = 0.2$ obtained by Tomasko et al. (1999) from Pathfinder images of the Martian sky was used. The results are presented in Figs. 8 and 9 (dark grey dots).

To understand how the change in size distribution parameters influences the result, the modeling was performed for the following range of size distribution parameters: $r_{eff} = 1.5$–1.8 μm and $v_{eff} = 0.2$–0.5. The values of r_{eff} lower than 1.5 μm are not considered because in dust storm conditions we should expect larger particles as it was mentioned by Wolff et al. (2006). The decrease of r_{eff} as well as the increase of v_{eff} cause a slight shift towards smaller values of w_1 and g_1 (Fig. 10).

It is clear that only a part of g_r and w_r solutions, obtained at step one, can be connected with the realistic values of the dust refractive index. Below we refer to this set of solutions as g_{r0} and w_{r0}. The low values of both the w_r and g_r appeared to be unrealistic. The small values of w_1 are rather associated with large absorptive particles with strongly asymmetric phase function characterized by a high value of g_1.

In the third step, the same modeling as at step two, but for the wavelength $\lambda = 213$ nm, was performed. The obtained values w_2 and g_2 are presented in Figs. 8 and 9 by light grey dots.

In the fourth step of our analysis, we tried to estimate the values of single scattering albedo w_b and asymmetry factor g_b at 213 nm, the short-wavelength end of the measured spectrum. The w_b and g_b were modeled for the dust particle size distribution used at step 2. The Mie theory was used. The refractive index was considered as wavelength independent in the wavelength range 200–300 nm and the 300 nm value was used. This was derived by comparing the results of step one and step two. For each value of w_{r0} and g_{r0} the values of w_1 and g_1 which deviate from them by less than 5% were sought. The values of the refractive index which correspond to the located values w_1 and g_1 are presented in Fig. 11. The values of w_b and g_b are marked in Figs. 8 and 9 by squares and triangles.

The last step is an attempt to estimate the dust cloud optical thickness. As it was shown above (Figs. 3 and 4), the presence of the dust cloud only slightly changed the radiance factor at $\lambda = 300$ nm but the I/F decreased significantly at shorter wavelengths and was therefore sensitive to the dust optical thickness. The radiance factor at $\lambda = 213$ nm, S_b, was fitted by the radiative transfer model using the optical parameters τ, w and g from Table 1. The Henyey–Greenstein phase function was used. As the value of the surface albedo A_b at 213 nm is not known, the calculations were done for a few values of A_b which were assumed to be smaller than or equal to the value of A_r. The result of the modeling is presented in Fig. 12 and Fig. 13 (case $A_b = 0.01$). The values of τ are represented by different intensities of grey color. The squares and triangles mark pairs w_{b0} and g_{b0} which were obtained on step four by extrapolating the refractive coefficient extracted at 300 nm to the wavelength 213 nm. They correspond to $\tau_b = 2.5 \pm 0.5$ for orbit 2284 and $\tau_b = 2.0 \pm 0.5$ for orbit 1902 (the uncertainty corresponds to variations of τ_b with w_{b0} and g_{b0}, see Figs. 12 and 13). The result appeared to be not very sensitive to the value of A_b due to the high dust loading. Below the influence of the surface albedo on the results will be considered in more details.

The following bounds of the dust optical parameters can be derived from the analysis presented above. The average value of the single scattering albedo w appears to be about 0.64 ± 0.04 at $\lambda = 300$ nm and decreases to 0.6 ± 0.045 at 213 nm. The asymmetry factor g is as high as 0.86 ± 0.03
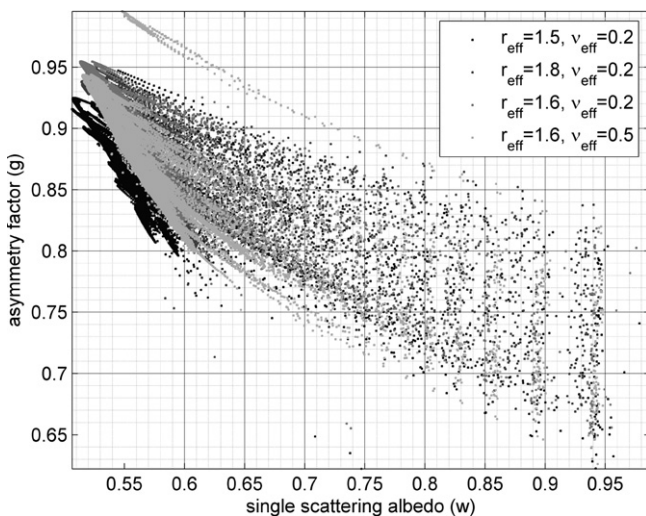

Fig. 10. The results of w and g modeling using the Mie theory and different dust particle size distributions.
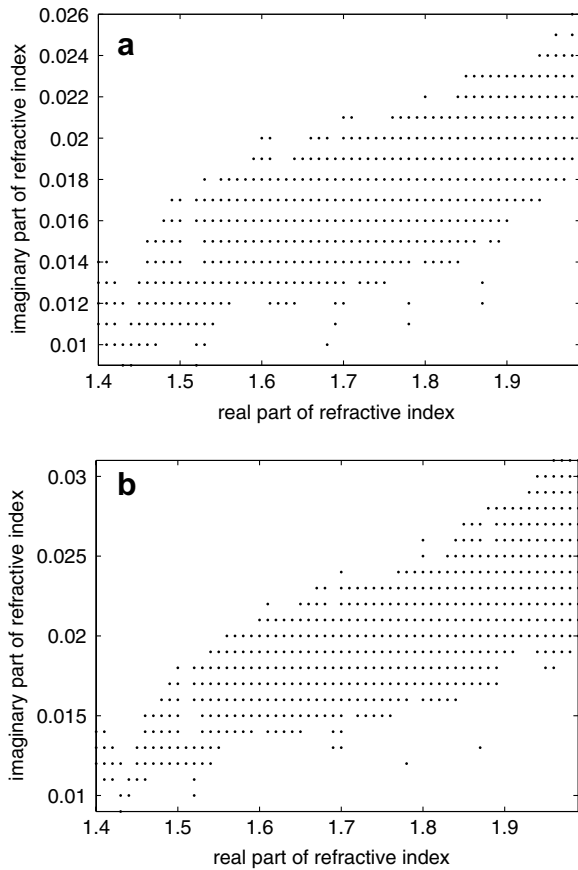
Fig. 11. The real (n) and imaginary (k) parts of the refractive index retrieved at step 4 (Fig. 5). n is restricted by values smaller than 2 and k – by values smaller than 0.1. (a) results for orbit 2284, (b) results for orbit 1902.

at 300 nm and slightly grows to 0.88 ± 0.04 at 213 nm. The uncertainties are derived from variations of the w_{r0}, g_{r0} and w_{b0}, g_{b0} values, (see Figs. 8 and 9).

The obtained dust optical parameters were used to retrieve the dust optical thickness for the entire dust storm events (Figs. 14 and 16 for orbits 2284 and 1902, respectively). The solid curves represent the radiance factor at $\lambda = 300$ nm, S_r, and the dashed curves represent the radiance factor at $\lambda = 213$ nm, S_b. Figs. 14b and 16b show the emission angles and SZAs of measurements for orbits 2284 and 1902, respectively. The surface albedo values (Figs. 15 and 17) were taken from the 300 nm albedo map and corrected for the opposition effect for all phase angles less than $25°$ (see Paper I for the details of the correction procedure). The same value of the dust optical thickness was used to fit the both the S_r and S_b curves. The following dust parameters were used: $w_r = 0.64$, $g_r = 0.86$ for orbit 2284, $w_r = 0.63$, $g_r = 0.88$ for orbit 1902, and $w_b = 0.6$, $g_b = 0.88$ for both orbits. We have to assume a little bit more absorptive at 300 nm aerosol with coarser grains for Hellas basin (orbit 1902) than for Argyre dust storm (orbit 2284) as it was discussed above.

It is interesting to consider how possible uncertainties in surface albedo values influence the result. To estimate this influence, a computation was performed using the same parameters as in Figs. 14 and 16 with a difference of $\pm 50\%$ in surface albedo. For the orbit 1902 the results of the modeling practically do not differ from the result presented in Fig. 16 due to both relatively high values of SZAs and high dust loading minimizing the surface albedo effect. There were much lower SZAs during the orbit 2284 and the effect of surface albedo variations was obvious (Fig. 18).
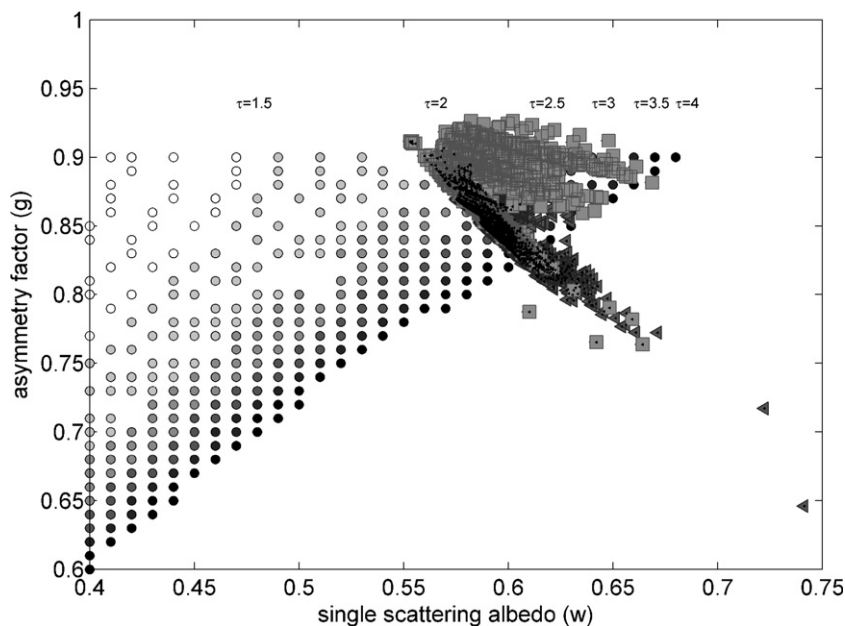

Fig. 12. Orbit 2284: circles represent the multiple solutions w_b, g_b ($\lambda = 213$ nm) retrieved from S_b (see Fig. 7, step 5). τ_b is presented by the intensity of grey color. The values of w_{b0}, g_{b0} obtained at step 4 (Fig. 7) are presented by light grey squares (real part of the refractive index $n < 1.8$) and dark grey triangles ($n > 1.8$). Black points mark values of w_{b0}, g_{b0} with the refractive index imaginary part $k > 0.02$.
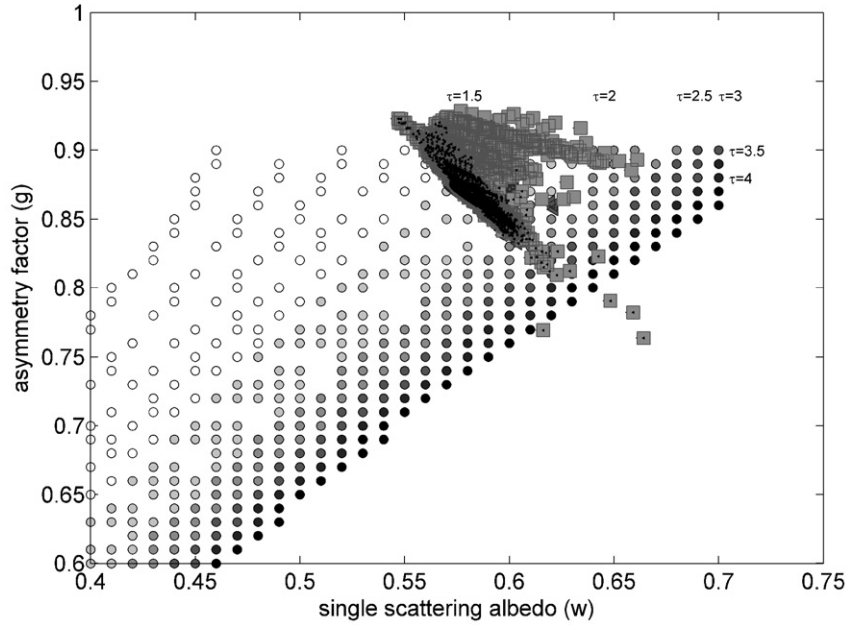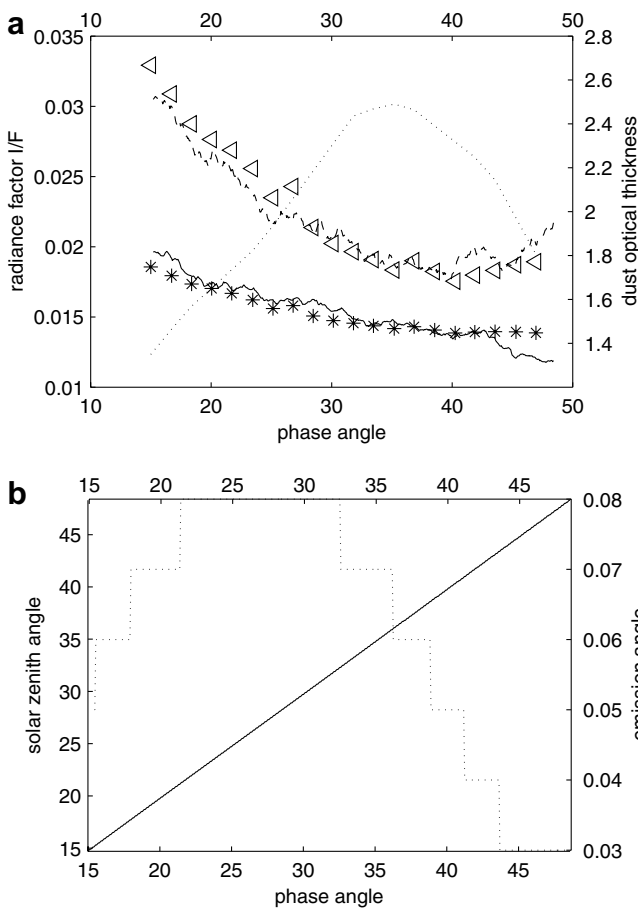
Fig. 13. The same as Fig. 12 for orbit 1902.

Fig. 14. Orbit 2284: (a) radiance factor S_r at $\lambda = 300$ nm (solid line) and S_b at $\lambda = 210$ nm (dashed line), the results of fitting are marked by asterisks (300 nm) and triangles (210 nm), dust optical thickness used for fitting the spectra is presented by a dotted line. (b) The observational geometry: solar zenith angle (solid line) and emission angle (dotted line).
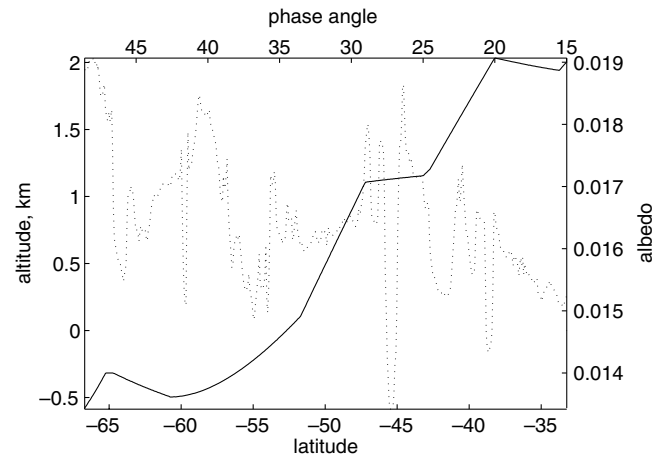

Fig. 15. Orbit 2284: the surface albedo (solid line) used for the fitting presented in Fig. 14a and the corresponding surface altitude (dotted line).

But the fitting results (Figs. 8 and 9) for the spectrum chosen for the analysis are still not affected by the surface albedo variation due to high dust loading.

6. Discussion

The analysis performed in the previous section has shown that although we cannot derive the exact values of the dust optical parameters, it is possible to derive some constraints of them. The obtained estimates ($w = 0.6 \pm 0.045$, $g = 0.88 \pm 0.04$ at $\lambda = 213$ and $w = 0.64 \pm 0.04$, $g = 0.86 \pm 0.03$ at $\lambda = 300$ nm) allow to conclude that w cannot be significantly smaller than 0.6 for a reasonable size distribution and tends to increase with wavelength while the g values show the opposite dependence. An important issue is the
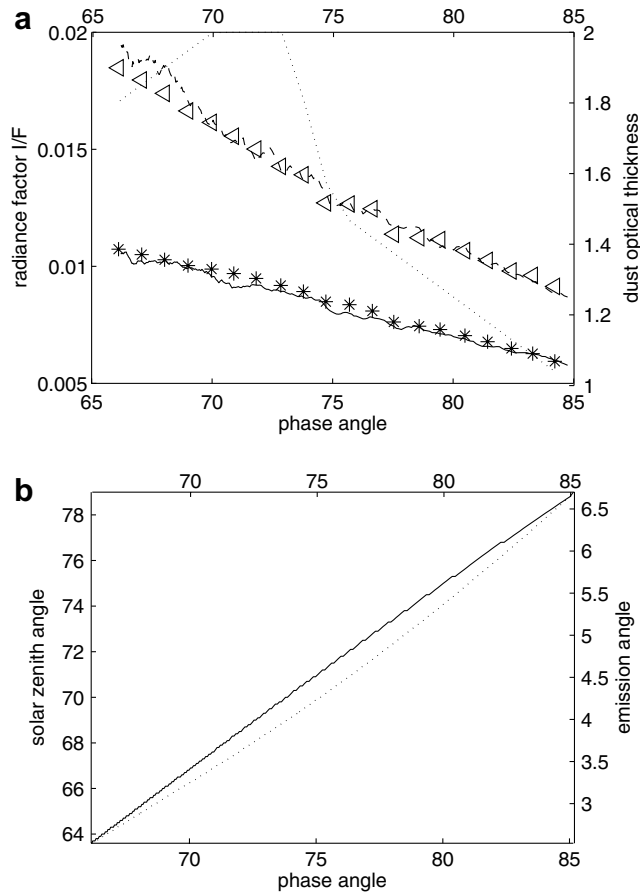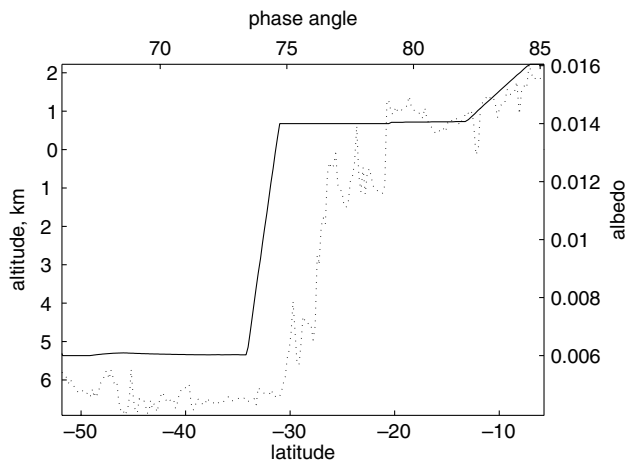
Fig. 16. The same as Fig. 14 for orbit 1902.

Fig. 17. Orbit 1902: the surface albedo (solid line) used for the fitting presented in Fig. 16a and the corresponding surface altitude (dotted line).
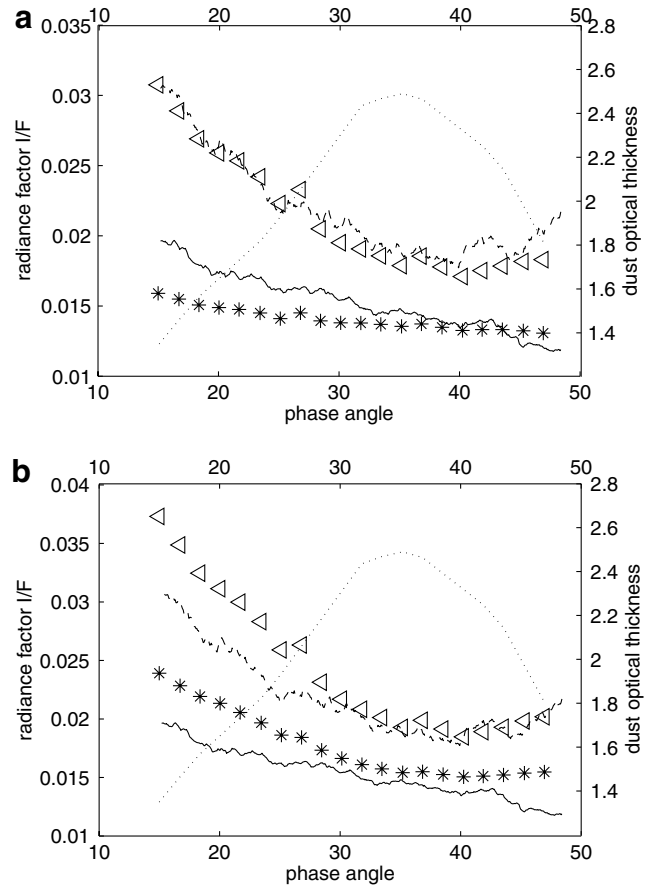

Fig. 18. (a) The same as Fig. 14a but the values of the surface albedo used in the fitting procedure (Fig. 15) were decreased by 50%, (b) the same as Fig. 14a but the values of the surface albedo used in the fitting procedure (Fig. 15) were increased by 50%.

observed change of the dust effect on the radiance factor I/F from an increase in the visible to a decrease in the UV.

The obtained estimates of w and g bring a correction to the Ockert-Bell et al. (1997) model of the Martian dust optical properties. According to their model $w_{ob} = 0.61$, $g_{ob} = 0.88$ at $\lambda = 300$ nm and $w_{ob} = 0.72$, $g_{ob} = 0.81$ at $\lambda = 210$ nm. Here, we show that both quantities w and g

have an opposite wavelength dependence in the considered wavelength domain. In Ockert-Bell et al. (1997), the Martian dust optical properties were derived assuming that the bright Martian soil has the same complex refractive index as the Martian dust. Hapke (1986) theory was used to relate the surface albedo to the refractive index. The UV surface albedo was derived from telescopic observations. But as we can see from Fig. 3 the reflectance in the UV grows significantly at $\lambda = 210$ nm due to a strong Rayleigh scattering on air molecules. The effect of the Rayleigh scattering should be removed very carefully to retrieve the correct value of the surface albedo which implies that the precise knowledge of the surface pressure is necessary. The underestimate of the Rayleigh scattering effect causes significant overestimate of the surface albedo. This may be the reason why the Ockert-Bell et al. (1997) obtained much less absorptive dust at $\lambda = 210$ nm than it was obtained in this paper.

Wolff et al. (1997) estimated w as 0.57 at $\lambda = 200$–300 nm, analyzing HST images. The same value was obtained by Wolff et al. (1999) for $\lambda = 410$ nm by fitting the HST images of a dust storm in Valles Marineris. In both papers the dust phase function (with $g = 0.55$) derived

by Clancy and Lee (1991) from Viking orbiter emission-phase-function measurements was used. The obtained value of w is lower than the results of this paper probably due to a lower value of g used in their analysis.

Pang et al. (1976) and Pang and Ajello (1977) studied the Mariner 9 'spot' pointing measurements of the 1971 Mars dust storm in the UV domain. Their estimate of the real component of the refractive index was $n > 1.8$ and the imaginary one $k = 0.01$–0.02. The values of k are quite consistent with our results (see Fig. 11). The same figure shows that the values of n obtained in this work can be lower than 1.8.

Goguen et al. (2003) analyzed optical properties of Martian dust from HST spectra of Mars during the 2001 dust storm. The values of w and g in the UV were modeled using the Mie theory. The Pathfinder dust model (Tomasko et al., 1999) was used. The following estimates of optical parameters were reported for the 220–305 nm wavelength range: $\tau = 2.0$, $w = 0.64$, $g = 0.84$. The imaginary part of the refractive index in the UV was taken $k = 0.02$. These estimates are quite close to the results of this paper.

In general, all measurements give a value of w close to 0.6. Some discrepancies between the results obtained by different authors may arise due to a non-unique solution in case of a simultaneous retrieval of the three parameters τ, w, and g.

7. Summary

In this work, we have presented exceptional nadir observations of the SPICAM UV spectrometer on Mars Express. Two dust storms: one, occurred on October 24, 2005, near Argyre Planitia and the other, occurred on July 9, 2005, in Hellas Planitia, were analyzed. The spectral domain 210–310 nm was considered. The measured UV spectra were divided in spectral sub-domains which were modeled for a wide range of dust optical thicknesses τ, single scattering albedos w and asymmetry factors g, using a multiple-scattering radiative transfer code. The dust optical parameters τ, w and g were also modeled using the Mie theory and a gamma distribution for dust particle size (Tomasko et al., 1999; Wolff et al., 2006). The comparison of the obtained values of τ, w and g with the results of the Mie modeling allowed to obtain some constraints for the dust optical properties. The following estimates were obtained: $w = 0.64 \pm 0.04$ at $\lambda = 300$ nm decreasing to 0.6 ± 0.045 at 213 nm, $g = 0.86 \pm 0.03$ at 300 nm, slightly growing to 0.88 ± 0.04 at 213 nm, $\tau = 2.5 \pm 0.5$ for the dust storm near Argyre basin (orbit 2284) and $\tau = 2.0 \pm 0.5$ for the dust storm in Hellas basin (orbit 1902). The obtained values are consistent with HST and Mariner 9 results.

Acknowledgments

References

Bell III, J.F. Iron, sulfate, carbonate, and hydrated minerals on Mars, in: Dyar, M.D., McCammon, C., Schaefer, M.W. (Eds.), Mineral Spectroscopy: A Tribute to Roger G. Burns, 5. Geochemical Society Special Publication, pp. 359–380, 1996.

Bertaux, J.-L., Korablev, O., Perrier, S., et al. SPICAM on board Mars Express: instrument, operations, observing modes, and overview of typical results. J. Geophys. Res. 111, E10S90, doi:10.1029/2006JE002690, 2006.

Cantor, B.A., James, P.B., Caplinger, M., et al. Martian dust storms: 1999 Mars orbiter camera observations. J. Geophys. Res. 106 (E10), 23653–23687, 2001.

Clancy, R.T., Lee, S.W. A new look at dust and clouds in the Mars atmosphere: analysis of emission-phase-function sequences from global Viking IRTM observations. Icarus 93, 135–158, 1991.

Clancy, R.T., Sandor, B.J., Wolff, M.J., et al. An intercomparison of ground-based millimeter, MGS TES, and Viking atmospheric temperature measurements: seasonal and interannual variability of temperatures and dust loading in the global Mars atmosphere. J. Geophys. Res. 105, 9553–9572, 2000.

Clancy, R.T., Wolff, M.J., James, P.B. Minimal aerosol loading and global increases in atmospheric ozone during the 1996–1997 Martian northern spring season. Icarus 138, 49–63, 1999.

Conrath, B.J. Thermal structure of the Martian atmosphere during the dissipation of the dust storm of 1971. Icarus 24, 36–46, 1975.

Evans, K.F. The spherical harmonics discrete ordinate method for three-dimentional atmospheric radiative transfer. J. Atm. Sci. 55, 429–446, 1998.

Forget, F., Hourdin, F., Fournier, R., et al. Improved general circulation models of the Martian atmosphere from the surface to above 80 km. J. Geophys. Res. 104 (E10), 24155–24176, 1999.

Goguen, J.D., Clancy, R.T., Wolff, M.J. et al. UV Optical Properties of Aerosol Dust from HST STIS Spectra of Mars during the 2001 Dust Storm, DPS 35th Meeting, 1-6 September 2003, Bulletin of the American Astronomical Society, 35 #4.

Hapke, B. Bidirectional reflectance spectroscopy. 4. The extinction coefficient and the opposition effect. Icarus 67, 264–280, 1986.

Lemmon, M.T., Wolff, M.J., Smith, M.D., et al. "Atmospheric imaging results from the Mars exploration rovers: spirit and opportunity". Science 306, 1753–1756, 2004.

Liou, K.N. An Introduction to Atmospheric Radiation, second ed Academic Press, San Diego, pp .83, International Geophysics Series, vol. 84, 2002.

Malin, M.C., Edgett, K.S., Davis, S.D. et al., Malin Space Science Systems Mars Orbiter Camera Image Gallery <http://www.msss.com/moc_gallery/>, 2006.

Mateshvili, N., Fussen, D., Vanhellemont, F., et al. Martian ice cloud distribution obtained from SPICAM nadir UV measurements. J. Geophys. Res. (Paper I) 112, doi:10.1029/2006JE002827, 2007.

Mishchenko, M.I., Travis, L.D., Kahn, R.A., et al. Modeling phase functions for dustlike tropospheric aerosols using a shape mixture of randomly oriented polydisperse spheroids. J. Geophys. Res. 102, 16831–16847, 1997.

McKim, R. Mars in 2005: first interim report. J. Br. Astron. Assoc. 116 (1), 6, 2006.

Montmessin, F., Quemerais, E., Bertaux, J.L., et al. Stellar occultations at UV wavelengths by the SPICAM instrument: retrieval and analysis of Martian haze profiles. J. Geophys. Res. 111, E09S09, doi:10.1029/2005JE002662, 2006.

Ockert-Bell, M.E., Bell, J.F., Pollack, J.B., et al. Absorption and scattering properties of the Martian dust in the solar wavelengths. J. Geophys. Res. 102, 9039–9050, doi:10.1029/96JE03991, 1997.

Pang, K., Ajello, J.M. Complex refractive index of Martian dust: wavelength dependence and composition. Icarus 30, 63–74, 1977.

Pang, K., Ajello, J.M., Hord, C.W., et al. Complex refractive index of Martian dust: Mariner 9 ultraviolet observations. Icarus 27, 55–67, 1976.

Perrier, S., Bertaux, J.L., Lefevre, F., et al. Global distribution of total ozone on Mars from SPICAM/MEX UV measurements. J. Geophys. Res. 111, E09S06, doi:10.1029/2006JE002681, 2006.

Tomasko, M.G., Doose, L.R., Lemmon, M., et al. Properties of dust in the Martian atmosphere from the imager on Mars Pathfinder. J. Geophys. Res. 104, 8987–9008, 1999.

Wolff, M.J., Lee, S.W., Clancy, R.T., et al. 1995 observations of Martian dust storms using the Hubble Space Telescope. J. Geophys. Res. 102 (E1), 1679–1692, 1997.

Wolff, M.J., Bell, J.F., James, P.B., et al. Hubble Space Telescope observations of the Martian aphelion cloud belt prior to the Pathfinder. J. Geophys. Res. 104 (E4), 9027–9041, 1999.

Wolff, M.J., Smith, M.D., Clancy, R.T., et al. Constraints on dust aerosols from the Mars exploration rovers using MGS overflights and Mini-TES. J. Geophys. Res. 111, E12S17, doi:10.1029/2006JE002786, 2006.